RESEARCH ARTICLE

ADVANCED OPTICAL MATERIALS
www.advopticalmat.de

Terahertz Volume Plasmon-Polariton Modulation in All-Dielectric Hyperbolic Metamaterials

Stefano Campanaro, Luca Bursi, Stefano Curtarolo,* and Arrigo Calzolari**

The development of plasmonics and related applications in the terahertz range faces limitations due to the intrinsic high electron density of the standard metals. All-dielectric systems are profitable alternatives, which allows for customized modulation of the optical response upon doping. Here, plasmon-based hyperbolic metamaterials are realized stacking doped III-V semiconductors that have been shown to be optically active in the terahertz spectral region. By using a multi-physics multi-scale theoretical approach, the role of doping and geometrical characteristics (e.g., thickness, composition, grating) in the modulation of high-*k* plasmon-polariton modes across the metamaterial is unraveled.

1. Introduction

Hyperbolic metamaterials (HMMs) are artificial systems characterized by extreme optical anisotropy as they behave as metals in one direction and as dielectrics in the perpendicular direction.[1,2] This implies that their dispersion relation [$\omega(\mathbf{k}) = costant$] is geometrically described by an open-surface hyperboloid and not by a closed ellipsoid, as in the case of ordinary materials. As such, HMMs can sustain extraordinary electromagnetic (EM) traveling modes with high-*k* wavevectors,[3] whose propagation is fully described by classical electrodynamics, once the dielectric functions of the composing materials are known. Usually, HMMs are realized through stacked alternation of metallic (e.g., Au, Ag, Cu, TiN) and dielectric (e.g., TiO_2, ZnO, Al_2O_3) layers, and the high-*k* modes are the Bloch modes of the metal-dielectric superlattice. They are volume plasmon-polaritons (VPPs) able to propagate along sharp cones across the stack[4] that arise from the resonant coupling of surface plasmon-polaritons (SPPs) at each metal/dielectric interface.[5] These unique optical properties make HMMs suitable candidates for many advanced optical applications like super-resolution imaging,[6] plasmonic sensors,[7,8] new stealth technologies,[9,10] and thermal emitters.[11,12]

The majority of HMMs realized in the last years are hyperbolically active in the near-infrared (IR) to ultraviolet (UV) spectral range (see e.g., Refs. [13–20]). However, it would be of great technological interest having HMMs working in the terahertz (THz) region, from 300 GHz to 10 THz. This would bridge the gap between electronics and optics, traditionally challenging for THz radiation generation, confinement, and detection.[21,22] Terahertz technology holds substantial potential for a broad range of emerging applications in the fields of non-destructive material inspection and quality control,[23] medical diagnostics,[24] imaging,[25] defense and security.[26]

Because of the intrinsic high electron density (e.g., $n_e \sim 10^{22} - 10^{23}$ cm^{-3}), plasmonic metals – including noble metals,[27] transition metal nitrides,[28–30] and high entropy carbides[31–33] – are not suited to achieve the THz region, having the (screen) plasmon resonance in the near-IR or visible range. The large carrier densities of metals also lead to significant ohmic losses and offer limited spectral tunability, further hindering their use in low-frequency HMM platforms. On the contrary, all-dielectric metamaterials represent a profitable alternative, where the conductive components are realized by doped semiconductors that have lower (e.g., $n_e \sim 10^{18} - 10^{20}$ cm^{-3}) and controllable electron densities. Doped semiconductors offer reduced ohmic losses, and allow for full compatibility with high-quality epitaxial growth. In particular, narrow-gap III-V semiconductors (such as InAs and InSb) are well suited for THz and mid-IR plasmonics,[34–38] thanks to their low effective masses, high mobility, and the strong tunability of their plasmonic response through doping,[39] temperature,[40] and electric fields.[41] Recent experimental reports[42–44] have demonstrated the possibility to realize hyperbolic metamaterials in the mid-IR and THz

S. Campanaro, L. Bursi
Dipartimento di Fisica, Informatica e Matematica
Università degli Studi di Modena e Reggio Emilia
Modena, Italy
E-mail: luca.bursi@unimore.it

S. Curtarolo, A. Calzolari
Department of Mechanical Engineering and Materials Science
Duke University
Durham, NC, USA
E-mail: stefano.curtarolo@duke.edu; arrigo.calzolari@nano.cnr.it

S. Curtarolo, A. Calzolari
Center for Extreme Materials
Duke University
Durham, NC, USA

A. Calzolari
Istituto Nanoscienze CNR-NANO-S3
Modena, Italy

The ORCID identification number(s) for the author(s) of this article can be found under https://doi.org/10.1002/adom.202502680

DOI: 10.1002/adom.202502680

frequency range, by using III–V semiconductor-based multilayers, highlighting the technological potential of this materials platform.

More generally, while realization of all-dielectric metamaterials has been experimentally proved,[42–49] their theoretical characterization remains more subtle. Indeed, the optical properties of semiconductors are system-specific and strongly depend on the growth conditions (e.g., composition, doping, defect concentration, etc.). Thus, the dielectric function is obtained through experimental means, otherwise modeling the high-*k* modes in all-dielectric HMMs would be impossible. Furthermore, even when experimental permittivities are available, they cannot be directly transferred to predict the hyperbolic response of other, albeit similar, compositions. On the theoretical side, while a few reports evaluate the plasmonic properties of doped semiconductors through simulations from first-principles that take explicitly into account the role of composition and doping modulation,[50–53] the ab initio description of HMMs remains limited to the homogenized medium treatment of the dielectric function.[54,55,56] This effective model does not include the effects of structural parameters (such as number of layers, thickness, grating coupler) that are crucial for the characterization and the prediction of the extraordinary waves within the metamaterials. This highlights the need for new theoretical approaches that combine materials science, quantum optics, and electromagnetism, where: **i**. the description of materials goes beyond the use of single empirical parameters (e.g., dielectric constant) tabulated for the reference bulk materials; and **ii**. the structural setup and the interface with the external environment are explicitly considered.

In this article, we attempt to bridge the gap between the experimental observations and the microscopic understanding of HMMs, by exploring their intrinsic properties. We systematically investigate metamaterials composed entirely of binary III-V semiconductors, demonstrating: **i**. their feasibility in realizing HMMs active in the THz, **ii**. their optical modulation with doping and multilayer geometry. We also provide a comprehensive theoretical analysis of VPP modes, offering insights into how these metamaterials can be engineered to achieve desired optical characteristics. In particular, we implemented a multiscale approach that combines the microscopic descriptions of materials with the macroscopic representation of traveling EM waves, integrating atomistic first principles simulations, effective medium theory, photonic band structure analysis, and continuum EM techniques based on scattering matrix method.

This research aims to advance the understanding of HMMs design principles, by enriching the EM description of VPP modes with system-tailored materials properties. The resulting critical insights could drive the optimization of semiconductor-based HMMs for applications in areas such as optoelectronics, sensing, and thermal management in the THz region.

2. Theoretical Methods and Computational Details

2.1. Materials Characterization

Atomistic simulations based on density functional theory (DFT) were carried out to calculate the electronic structure and the complex dielectric functions of both undoped and doped III-V semiconductors. All simulations were performed using the DFT engine (*pw.x*) included within the Quantum ESPRESSO (QE) suite.[57,58] PBE generalized gradient approximation[59] was applied to the exchange-correlation functional. Electron-ion interactions were described using norm-conserving pseudopotentials[60] from the ONCVSP library.[61] Single-particle wavefunctions were expanded in planewaves with a kinetic energy cutoff of 120 Ry. A uniform mesh of (16 × 16 × 16) **k**-point was used to sample the Brillouin zone in self-consistent DFT cycles, and a denser (60 × 60 × 60) **k**-grid was exploited in non-self-consistent field calculations needed for optical properties. Lattice parameters were optimized using the variable-cell minimization method. All structures were fully relaxed by using a total-energy-and-force optimization scheme, until forces per atom are less than 0.03 eV/Å. Undoped semiconductors were simulated in the primitive *fcc* cell, while Si-doped InAs systems were modeled with periodic supercells of different sizes (see Section Results). The well-known DFT underestimation of energy band gap was corrected by using a pseudo-hybrid Hubbard implementation of DFT+U within the Dudarev formulation,[62] namely ACBN0,[63,64] which involves the use of the effective parameter $U_{eff} = U - J$, where U is the corrective Hubbard term and J accounts for the energy cost associated with the exchange interaction. The ACBN0 approach is implemented in the PAOFLOW code,[65] which operates in a joint loop with the DFT-based executables of QE. The calculated U_{eff} values for each chemical species are collected in Table S1 (Supporting Information).

The complex dielectric function $\hat{\varepsilon}(\omega) = \varepsilon_1 + i\varepsilon_2$ is evaluated using the code *epsilon.x*, also included in the QE suite. This code implements an independent particle formulation of the frequency-dependent (ω) Drude-Lorentz model for solids,[66,67] which explicitly includes both intraband and interband transitions between Bloch states, along with Drude-like and Lorentz-like relaxation terms, which account for the finite lifetime of the electronic excitations and the effects of the dissipative electron scattering.[68]

2.2. Effective Medium Theory (EMT)

Effective medium theory[69] is used to describe the overall optical properties of a periodically repeated (i.e., infinite) multilayer at the macroscopic level. Under this approximation — valid when the thickness of each constituent layer is much smaller than the wavelength of the probing radiation — the effective dielectric functions in the directions parallel ($\epsilon_{\parallel}$) and perpendicular ($\epsilon_{\perp}$) to the optical axis (**Figure 1a**) are:

$$\varepsilon_{\perp} = f_m \varepsilon_m + f_d \varepsilon_d \,, \tag{1}$$

$$\varepsilon_{\parallel} = \frac{\varepsilon_m \varepsilon_d}{f_d \varepsilon_m + f_m \varepsilon_d} \,, \tag{2}$$

where ϵ_m (ϵ_d) is the complex dielectric function of the metallic (dielectric) material resulting from DFT+U calculations; f_j ($j = \{m, d\}$) is the layer filling factor defined as $f_j = d_j/d_{tot}$ where $d_{tot} = d_m + d_d$ is the thickness of the periodic unit cell (Figure 1a). The macroscopic conditions for VPP excitation and the angle between the extraordinary wave and the optical axis are analysed through the angular dielectric function ϵ_{φ} and the angle Θ, which are geometrical functions of $\epsilon_{\parallel}$ and $\epsilon_{\perp}$; see Section S1 (Supporting Information).

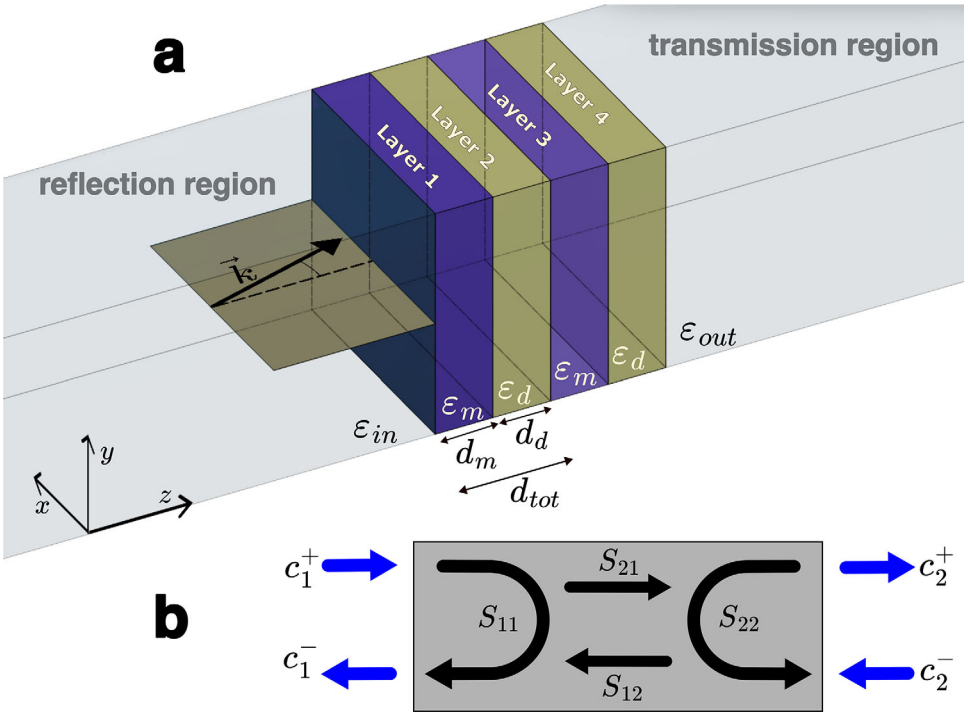

Figure 1. a) Schematic representation of a finite stacked metamaterial composed of alternating metallic (m) and dielectric (d) layers, each characterized by its dielectric function ϵ_j and thickness d_j, where $j = \{m, d\}$. Gray regions indicate the embedding media for reflection and transmission, also characterized by the respective dielectric functions ϵ_{in} and ϵ_{out}. The optical axis is aligned along the z direction. b) Scattering matrix formulation for a single layer. Forward (c_1^+, c_2^+) and backward (c_1^-, c_2^-) propagating wave amplitudes are related through the elements S_{ij} of the scattering matrix.

2.3. Scattering Matrix Method (SMM)

The VPP propagation through a finite 3D multilayer[70,71] is described through the scattering matrix (S-matrix),[72] as implemented in the *AFLOW-EMERALD* code.[73] By simulating finite multilayers with a defined number $\mathcal{N}$ of periods, *AFLOW-EMERALD* provides the reflectivity, transmissivity, and absorption of EM waves across the stack, accounting for the interference effects at each interface and resonant phenomena due to the internal structure of the superlattice, as well as the coupling with the external environment. For non-magnetic materials, the scattering matrix is calculated for each layer and depends on the frequency of incident monochromatic radiation, its planar wavevector (k_x), and the dielectric permittivity ($\hat{\epsilon}$) that we obtained from DFT+U simulations. The matrix $\boldsymbol{S}$ relates the amplitude coefficients of the forward (c^+) and backward (c^-) propagating components of the electric and magnetic fields at the left (1) and right (2) interfaces of the n-th layer, as illustrated in Figure 1b. The reflectivity (R), transmissivity (T), and absorption (A) functions are calculated from the resulting EM fields being reflected, transmitted, and absorbed through the entire multilayer;[73] see Section S1 (Supporting Information) for further details.

2.4. Photonic Band Structure (PBS)

The Bloch modes of periodic metal-dielectric superstructures are studied through the evaluation of the photonic band structure, whose formulation is derived from photonic crystal theory.[74] The 3D translational invariance of the periodic multilayers implies that the dielectric function is also invariant under translation by Bravais vectors $\mathbf{R}$, i.e., $\epsilon(\mathbf{r} + \mathbf{R}) = \epsilon(\mathbf{r})$. This leads to the validity of the Bloch–Floquet theorem and the formation of allowed (photonic bands) and forbidden (photonic gaps) EM states. Photonic band structures are calculated with the *AFLOW-EMERALD* code[73] by expanding the electric and magnetic fields on a planewaves basis set, as detailed in Section S1 (Supporting Information). The dielectric function is derived from the first principles simulations of the composing bulk materials.

3. Results

The theoretical approaches employed in this work operate at complementary levels and together provide a coherent multiscale description of the metamaterials. EMT, informed by the material dielectric functions computed from first principles, offers a macroscopic picture of an infinite multilayer, described as a single, homogenized medium, and predicts the spectral regions in which the system behaves as Type-I, Type-II HMM, or as a dielectric. SMM extends the analysis to finite stacks, explicitly accounting for interface reflections, grating-assisted momentum matching, and coupling to the external environment, thus enabling the description of the propagation of EM waves through realistic metamaterials. Finally, PBS analysis identifies the allowed Bloch modes of the periodically repeated multilayer and rationalizes which modes can be excited under the boundary conditions imposed by the finite-thickness stack and the matching coupler. Here, we considered ideal interfaces, this approximation can be

systematically relaxed at different levels of the multiscale framework. The hierarchical use of EMT, SMM, and PBS enables us to connect material properties with propagating VPP modes in tailor-made metamaterial structures.

3.1. Optical Proprieties of Multilayer Components

Along the lines of the experimental structures described in Refs. [42, 43], we have modeled the HMMs as binary superlattices composed of alternating layers of dielectric (III-V semiconductors) and metallic (Si-doped InAs) materials, stacked along the z axis. A schematic representation of an all-dielectric HMM multilayer is shown in Figure 1a. In the experiments of reference, the range of interest of the electromagnetic radiation was $\lambda \sim (2-20)\mu$m (i.e., THz to mid-IR range) and the thickness of the building layers within the stack was of the order of 100 nm. Since the wavelength of the incoming radiation is much greater than the thickness of the individual components, the homogenization assumptions[69] are largely satisfied, quantum confinement effects can be neglected, and the complex dielectric functions of the single bulk materials are sufficient to fully characterize the optical response of the overall metamaterials.

As first step, we evaluated electronic and optical properties of the nine III-V binary semiconductors (namely, AlP, AlAs, AlSb, GaP, GaAs, GaSb, InP, InAs, and InSb) in the *fcc* zincblend phase. The resulting lattice parameters (a_0) and the band gap values (E_g) are summarized in Table S1 (Supporting Information). The results indicate that the DFT+U approach correctly reproduces the semiconducting behavior ($E_g > 0$) of all the systems, including narrow-gap semiconductors, such as InAs, that result semimetallic ($E_g < 0$) in standard DFT calculations.[75] The band gap underestimation is significantly reduced with the DFT+U correction, albeit a residual underestimation remains for all systems. The corresponding band structure plots (see Section S2, Supporting Information) well agree with theoretical results obtained by using higher-level DFT approaches, such as hybrid functionals, or many-body GW approximation.[76,77] The frequency-dependent dielectric functions of the III-V semiconductors have been calculated by using a single-particle Drude–Lorentz approach.[78] The results of the simulations very well concur with previous theoretical calculations[79] and with experimental data.[80–82] The results for the nine III-V compounds are collected in Section S3 (Supporting Information). All the main spectral features of both ϵ_1 and ϵ_2 (i.e., peak energies and peak intensities) are accurately reproduced for all systems. Yet, with respect to the experimental data, we observe a small but systematic rigid redshift in the inter-band optical absorption threshold, which is reminiscent of the residual underestimation of the simulated energy band gap discussed above.

In line with the experimental case,[42,43] the metallic component in our multilayers is Si-doped InAs (Si:InAs) that we simulated at different Si concentrations in order to unravel the role of free charge density on the plasmon-polariton properties across the metamaterials. Si:InAs is modeled by including In-substitutional Si atoms in extended InAs supercells, within the virtual crystal approximation (**Figure 2a**). The doping concentration is defined as $c = N_{Si}/N_{In}$, where N_{Si} is the number of Si dopant atoms, and N_{In} is the total number of In atoms in an equivalent undoped supercell. In the experimental references,[42,43] doping concentration is determined in terms of the resulting free electron density $n_{el} \sim 10^{20}$ cm^{-3}, which corresponds to a nominal Si concentration $c \simeq 2.2\%$. Here, we generate three models (labeled **1**, **2**, and **3**) at varying doping concentrations in the range $1.6 - 3.7\%$, which includes the experimental case. The details relative to concentration and cell size are summarized in **Table 1**. After full atomic relaxation, the results indicate that Si imparts a slight local distortion in the structure that is almost insensitive to the doping concentration.

As expected, the ground state electronic structure of all models corresponds to an n-type degenerate conductor, as shown in Figure 2b, for the case of medium-doping model **2**. The density of states (DOS) of Si:InAs exhibits all the spectral features of undoped InAs. Yet, the pristine energy gap of the host is slightly reduced in the doped system, while no Si-derived peaks appear in the gap region. Si donates its extra *3p* electron to the host conduction band, without changing much the shape and the curvature of the conduction band minimum. As a consequence, doping causes a shift of the Fermi level into the conduction band, and the system acquires a metal-like behavior. The other two models show very similar DOS spectra, which differ only in the position of the Fermi level with respect to the bottom of the conduction band (ΔE_F in Table 1) that corresponds to a different injected charge, which increases with Si concentration. By inverting the Drude formula in the parabolic approximation, it is possible to estimate, a posteriori, the effective free electron density generated by doping. The results are of the order of $n_e \sim 10^{19}$ cm^{-3} for model **1**, and $n_e \sim 10^{20}$ cm^{-3} for models **2** and **3**, slightly lower than the nominal values but still in agreement with the experimental data.[42,43]

The dielectric functions of Si:InAs configurations have been calculated with the same computational procedure and the same parameters detailed above. Figure 2 shows the resulting plots for the real (panel c) and imaginary (panel d) parts of the dielectric functions as a function of the doping concentration. While the doping only marginally affects the optical properties above $E \sim 2$ eV, it completely changes the dielectric function in the low-energy part of the spectrum. At low frequencies (i.e., $E \to 0$), the optical properties of Si:InAs differ from the original InAs, being similar to a simple metal. E_p identifies the energy at which the real part of the dielectric function changes sign [$\epsilon_1(E_p) = 0$], i.e., the energy at which the system undergoes an optical switch from metal- to dielectric-like. This is a key parameter in the characterization of the hyperbolic properties of the metamaterials (see below). In all Si:InAs models, $\epsilon_2(E_p)$ is also negligible (Figure 2d). This corresponds to the possibility of exciting a collective electronic oscillation of a reduced part of the free-electron density, known as a screened plasmon resonance in the THz range. In this case, E_p represents the THz plasmon energy for the system. While for pure metals, E_p is an intrinsic property that cannot be changed, for doped-semiconductors the plasmon energy can be tuned by controlling the electron density, i.e., by changing the doping conditions (Table 1). Finally, it is worth noticing that the permittivity for low-doping concentration model (**1**) exhibits an extra peak at ~0.3 eV, absent in the other two doping models. This structure arises from residual interband transitions in lightly doped InAs, occurring just above the fundamental gap. As the doping level increases, the Fermi level moves deeper into

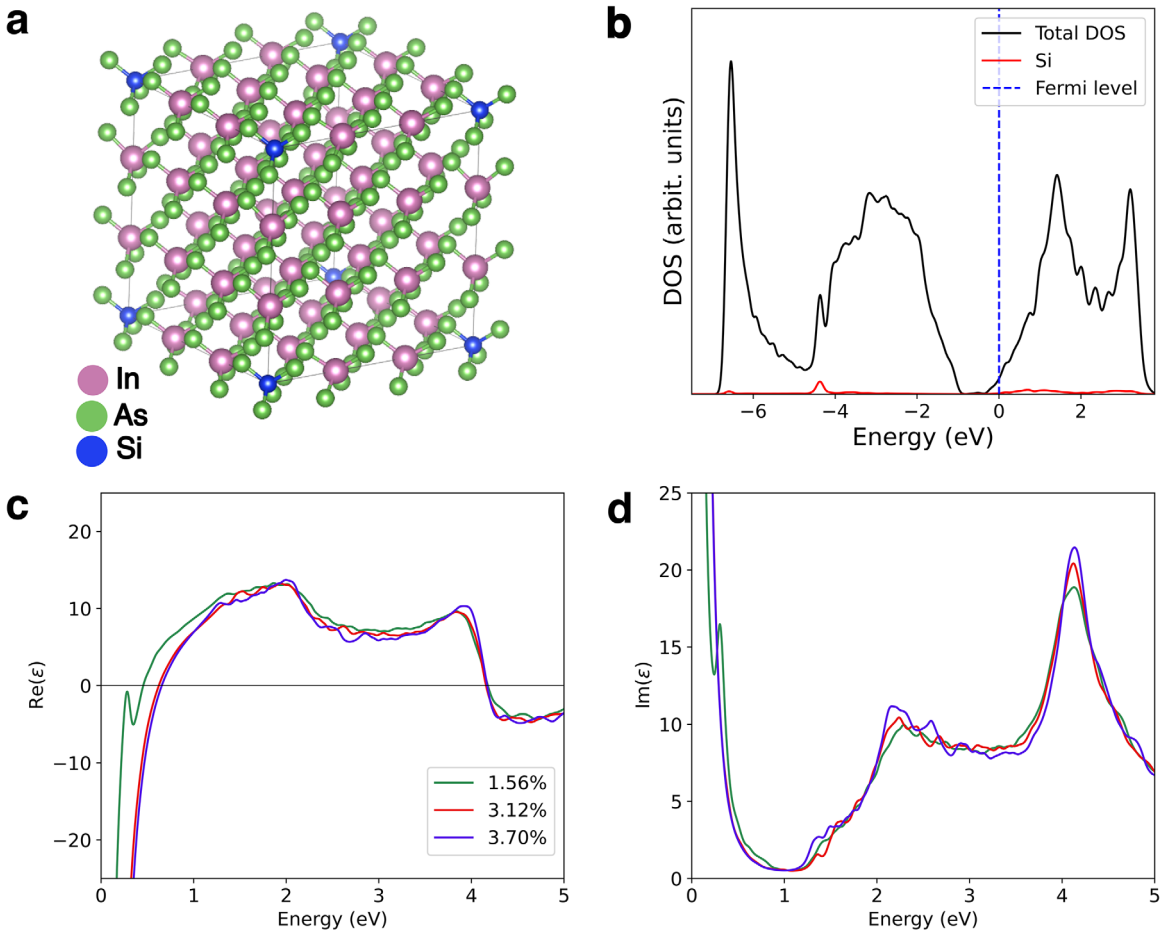

Figure 2. a) Atomic structure of Si:InAs supercell. b) Total (black line) and Si-projected (red line) density of states (DOS) of Si:InAs (model **2**). c) Real and d) imaginary parts of the dielectric function of Si:InAs as a function of Si concentration.

the conduction band, the Pauli blocking progressively suppresses these transitions, and the corresponding absorption feature naturally disappears at higher electron densities. The presence of this spectral feature does not change the plasmonic character of the Si:InAs model.

3.2. Hyperbolic Multilayers

By treating metamaterials as homogeneous, EMT predicts the hyperbolic behavior of the multilayers and the spectral features of the VPPs within the stacks. The optical properties of HMMs are evaluated by combining the bulk dielectric functions of the intrinsic III-V semiconductors (ϵ_d) and Si:InAs (ϵ_m) calculated from first principles. Equations (1-2) are used to compute the perpendicular ($\epsilon_\perp$) and parallel ($\epsilon_\parallel$) components of the effective dielectric tensor with respect to the optical axis (Figure 1a). Nine multilayers have been considered by mixing the III-V semiconductors with model **2** of Si:InAs. **Figure 3** shows the real (solid lines) and imaginary (dashed lines) parts of the parallel (red lines) and perpendicular (blue lines) dielectric functions of equal-composition ($f_m = f_d = 0.5$) Si:InAs/AlSb stack, taken as reference. The results for the remaining Si:InAs/III-V multilayers are summarized in Section S4 (Supporting Information).

Table 1. Si-dopant concentration (c), supercell lattice parameter (a_0), Si-In and Si-As nearest neighbors distances for the three Si:InAs models described in the text. ΔE_F is the energy difference between the Fermi level (E_F) and the bottom of the conduction band; E_p is the plasmon energy.

Model	c (%)	a_0 (Å)	Si-In (Å)	Si-As (Å)	ΔE_F (eV)	E_p (eV)
1	1.56%	24.23	4.24	2.41	0.12	0.46
2	3.12%	18.17	4.24	2.41	0.21	0.62
3	3.70%	12.12	4.24	2.41	0.25	0.65

The hyperbolic dispersion implies the condition $\epsilon_\perp \cdot \epsilon_\parallel < 0$. At low energy ($E < E_{II} = 0.44$ eV in Figure 3), Re[$\epsilon_\perp$] is dominated by ϵ_m and Re[$\epsilon_\parallel$] by ϵ_d. This implies that the perpendicular component (blue lines) has a metal-like behavior similar to Si:InAs, while the parallel component (red lines) has a typical dielectric character similar to those of the undoped semiconductor. Thus, the multilayer acts as Type-II HMM. In the range $E \in \{0.44 - 0.47\}$ eV, Re[$\epsilon_\perp$] has a zero, switching from negative to positive for all systems. This happens when Re[ϵ_m] = −Re[ϵ_d], which in turn corresponds to a maximum of $\epsilon_\parallel$. Beyond this resonance energy, Re[$\epsilon_\parallel$] decreases until it crosses the zero, switching sign

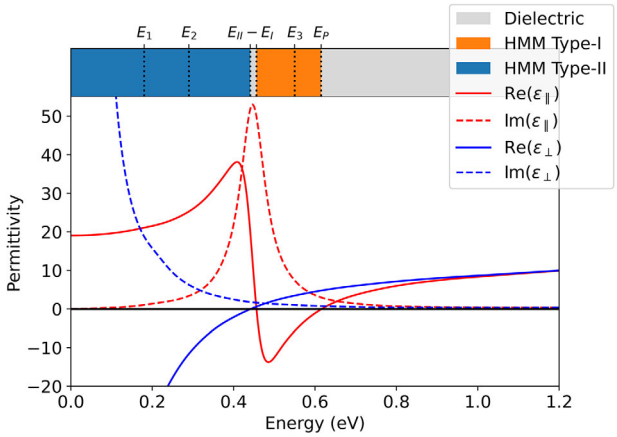

Figure 3. Real (solid lines) and imaginary (dashed lines) parts of the parallel (red lines) and perpendicular (blue lines) dielectric functions of Si:InAs/AlSb multilayer ($c_2 = 3.12\%$ and $f_m = 0.5$). Top bar indicates the spectral optical character of the multilayer – namely Type-I (orange) and Type-II (blue) hyperbolic, and dielectric (gray). Vertical dashed lines mark characteristics energies discussed in the text.

from positive to negative, with a typical Lorentz-like character. The energy value of the Lorentz resonance depends on the III-V semiconductor used as dielectric. For $E > E_I = 0.47$ eV the trend is inverted, with $\epsilon_\perp$ driven by ϵ_d and $\epsilon_\parallel$ by ϵ_m. As a consequence, $\epsilon_\parallel$ has a metal character, while $\epsilon_\perp$ has a dielectric behavior, corresponding to a Type-I HMM. For $E > E_p = 0.62$ eV, both components (III-V and Si:InAs) are dielectric-like, and the same holds for the multilayer.

A direct comparison with the experimental results of Refs. [42, 43] indicates that our theoretical spectra are in very good agreement with all the experimental features of the multilayer, including the alternation of the hyperbolic type character as a function of the radiation energy. For a better comparison with experimental data, Figure S11 (Supporting Information) reports the dielectric function of Figure 3) as a function of wavelength, instead of energy. Yet, our theoretical spectra are affected by a slight blueshift, when compared with the experiments. This minor discrepancy is mostly ascribable to: (i) the residual band gap underestimation of the pristine semiconductors calculated at the DFT+U level; (ii) the exact doping level, which may differ from the exact experimental value; (iii) the assumption of ideal, defectless interfaces in the theoretical modeling. Despite these minor details, the agreement with the experimental results confirms a posteriori the accuracy of the joint DFT+U/EMT approach used in this work.

The effects of composition, thickness, and doping on the hyperbolic behavior of the multilayers are illustrated in **Figure 4**. To better appreciate the differences in the optical properties of HMMs in the low energy part of the spectrum, these results are expressed in terms of wavelength (λ) instead of energy. The nine metamaterials (Figure 4a) exhibit a variable behavior as a function of the radiation wavelength. The hyperbolic character appears for $\lambda > \lambda_p = hc/E_p = 2.0\tilde{}\mu$m (i.e., $E < E_p = 0.62$ eV). All systems have a prevalent Type-II character (blue area), except for an intermediate range, where they exhibit a Type-I dispersion (orange area). The former type is correlated to the negative value of $\epsilon_\perp$, while the latter is associated with the Lorentz-like inversion of $\epsilon_\parallel < 0$. At shorter wavelengths ($\lambda < \lambda_p$), the radiation overcomes the plasma frequency of the metal, and the multilayer is globally dielectric (gray area). Since the plasmon energy of Si:InAs varies with the doping (Table 1), the hyperbolic range can be tuned by controlling the dopant concentration. An increase in the doping concentration (Figure 4b) imparts a blueshift of the plasma frequency that sets the transition between the hyperbolic and the elliptic (i.e., dielectric) dispersion behavior. In the case of $c_1 = 1.56\%$, and $f_m = 0.5$, the Si:InAs/AlSb multilayer exhibits only a Type-II character in the hyperbolic range. However, for metallic filling factors between 0.70 and 0.95, the system also develops narrow frequency intervals in which it displays a Type-I hyperbolic response. Supplementary plots (Figure S12, Supporting Information) – analogous to Figure 4c – for the lowest (c_1) and highest (c_3) doping concentrations confirm that the onset of Type-I and Type-II hyperbolicity depends on both doping level and metallic filling factor.

Figure 4c displays the trend associated with the variation of the composition filling factor f_m, which measures the amount of the metallic component within the multilayer: $f_m = 0$ ($f_m = 1$) corresponds to pure dielectric (metallic) system. For $\lambda > \lambda_p$, the actual hyperbolic range depends on the filling factor. In general, a metal/dielectric ratio of $\approx 40 - 60\%$ provides a wider spectral range with hyperbolic dispersion, which progressively reduces to longer wavelengths as much as one of the components becomes predominant. In summary, by controlling the chemical species, the doping, and the geometry of the stack it is possible to fine tune the optical character of the multilayers and achieve hyperbolic behavior across the near-IR to THz spectral range.

3.3. Volume Plasmon-Polaritons

The spectral analysis of VPP excitations is obtained from the angular dielectric function $\epsilon_\varphi(E)$ and the propagation angle $\Theta(\varphi)$, where E is the energy and φ is the angle between the wavevector of the incoming radiation $\mathbf{k}$ within the metamaterials and the optical axis z (see Section S1, Supporting Information, for further details). Here, we focus on the reference case of Si:InAs/AlSb multilayer (doping concentration $c_2 = 3.12\%$ and filling factor $f_m = 0.5$). Since ϵ_φ is a function of the energy of the incoming radiation, we selected a few representative energies (E_i) marked by vertical dashed lines in Figure 3. Energies $E_1 = 0.18$ eV and $E_2 = 0.29$ eV correspond to a Type-II hyperbolic character, while $E_3 = 0.55$ eV corresponds to a Type-I HMM.

In the case of E_1 and E_2, the real part of ϵ_φ is negative at small angles and it becomes positive beyond a critical angle φ_c, which increases when the energy is increased ($\varphi_{c1} < \varphi_{c2}$). The trend is inverted for E_3 where ϵ_φ is positive at small angles and changes sign at $\varphi_{c3} \sim 65°$. This behavior follows the distinct topology of the underlying hyperboloids that describe the dispersion isosurfaces –two-sheeted in the Type-I case and one-sheeted in the Type-II case. Indeed, the condition $\mathrm{Re}[\epsilon_\varphi] = 0$ determines the angular boundary between the metallic and dielectric response of the metamaterial (the analogous of plasmon excitation in bulk materials), and determines the critical angle φ_c that satisfies the wavevector refraction conditions at the interface between the metamaterial and the external environment (Figure 1a). For each energy, $\tan(\varphi_c) = k_z/k_x = \sqrt{\epsilon_\perp/\epsilon_\parallel}$ represents the asymptote

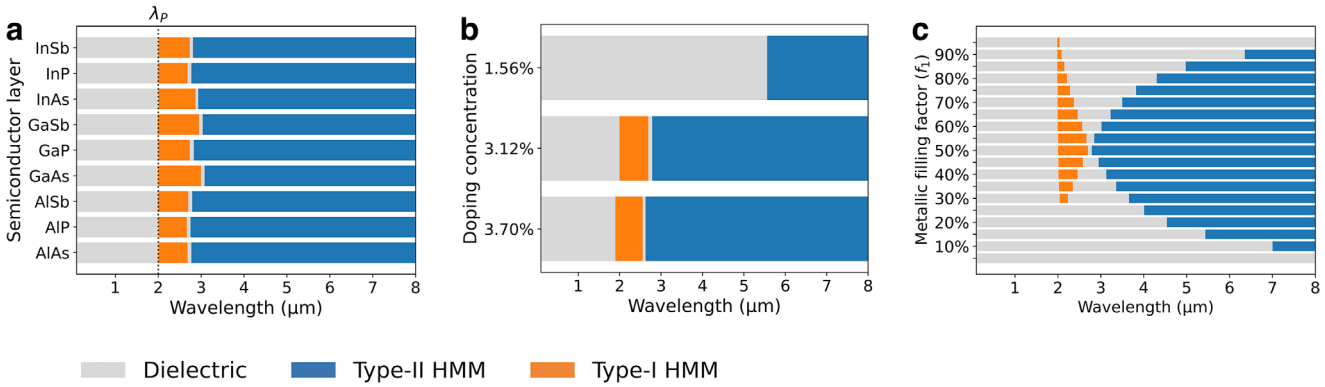

Figure 4. Spectral optical character – namely Type-I (orange) and Type-II (blue) hyperbolic, and dielectric (gray) – of HMMs composed of: a) III-V semiconductors/Si:InAs ($c_2 = 3.12\%, f_m = 0.5$) as a function of the dielectric component; b) Si:InAs/AlSb ($f_m = 0.5$) as a function of Si doping concentration; c) Si:InAs/AlSb ($c_2 = 3.12\%$) as a function of the filling factor f_m in the range (0.05 – 0.95)%.

to the hyperboloid that describes the dispersion isosurface of the metamaterial (**Figure** 5b). Thus, for a Type-I (Type-II) HMM, φ_c is the maximum (minimum) angle that the incoming radiation must have to propagate within the stack. As such, the three intersections φ_{ci} in Figure 5a correspond to the extreme geometrical conditions for the excitation of conic VPPs, whose angular radii are given by the corresponding Θ angles (Figure 5a, bottom panel). For all the considered energies, Θ is negative for all the allowed φ angles. This is the signature of the excitation of backward waves, where the Poynting vector **S** and the wavevector **k** are in opposite, lateral directions. This anomalous refraction effect is the basis for advanced transformation optics and EM cloaking applications.

In real experimental conditions, the angle φ is not a free variable but is dictated by the number of bilayers in the stack as well as by the matching setups (e.g., prism or grating) used to compensate the momentum mismatch between the incident radiation and the VPP. This means that, given the actual geometry of the overall system (HMM + coupler), only a few energies and specific angles φ may effectively excite a VPP. These aspects, along with the multiscattering effects deriving from the internal metal/dielectric interfaces, cannot be caught by EMT that considers the entire multilayer as a single homogenized medium. A proper description of these effects is necessary to be predictive in designing/optimizing customized heterostructures.

In order to overcome these limitations, we solved the electromagnetic problem of a finite multilayer composed of alternating metal/dielectric materials, by employing the scattering matrix method. This approach allows us to model the behavior of the EM waves that propagate through the metamaterial and to explicitly include the boundary conditions imposed by the grating layer. Along the line of the experimental samples,[42,43] we considered a metamaterial composed of $\mathcal{N} = 10$ periods of alternating Si:InAs/AlSb bilayers, with the following parameters: doping concentration $c_2 = 3.12\%$, filling factor $f_m = 0.5$, and thickness of a single bilayer $d_{tot} = 100$ nm (Figure 1a). The dielectric functions that characterize the individual layers are those calculated at the DFT+U level for the respective bulk materials. A gold grating layer with variable periodicities $\Lambda = 0.9$˜μm, 1.3 μm, and 1.8 μm, respectively, is introduced on top of the multilayer stack. The value $\Lambda = 1.8$ μm corresponds to the experimental condition used in Ref. [42]. The entire system – comprising both multilayer and grating – is embedded in air, modeled as a medium with dielectric constant $\epsilon = 1.0$.

Figure 6a shows the reflectivity spectra (R) calculated by varying the spacing of the grating coupler. In the hyperbolic energy range ($E < E_p = 0.62$ eV), the excitation of VPP modes corresponds to local minima in the reflectivity spectra. For example, in the case of $\Lambda = 0.9$ μm, three distinct resonances – labeled VPP0, VPP1, and VPP2 and marked with yellow symbols – can be identified. The corresponding transmittance and absorption spectra are reported in Figure S13 (Supporting Information). Resonance VPP0 occurs in the Type-I hyperbolic region, while VPP1 and VPP2 occur in the Type-II domain. Here, the hyperbolic character is derived from EMT (Figure 3a). The remaining minima for $E > E_p$ correspond to usual interband excitations in dielectrics. VPP0 has the most pronounced reflection minimum, hardly modified by the grating geometry. The increase in the grating period causes a reduction of the reflection dips. Even though these three VPP modes lie in the mid-IR, this does not limit the operational range of the HMM to the THz region. Indeed, these VPP energy values result from a specific combination of doping, stack geometry, and momentum-matching conditions imposed by the grating coupler. When the grating period is increased (especially for $\Lambda = 1.8$μm), the VPP branches associated with VPP1 and VPP2 undergo a redshift with respect to the $\Lambda = 0.9$μm case. These redshifted modes fall squarely in the mid-IR to THz range, in agreement with the experimental findings.[42,43]

For non magnetic HMMs, only transverse magnetic modes can be excited.[83] The magnetic fields profile corresponding to the three VPPs marked in Figure 6a are shown in **Figure** 7 (upper panel), which actually confirm that the EM waves propagate within the stack. However, only VPP0 wave propagates with significant intensity outside the multilayer, i.e., $H > 0$ in the region on the right. For VPP1 and VPP2, the front-grating allows for the excitation of the EM modes within the multilayer, while the low-k mismatch – typical of Type-II HMMs – prevents their transmission into the air region (see also the transmittance plot in Figure S13, Supporting Information). As a result, these modes can be excited but remain confined within the stack. A different external dielectric material or the inclusion of a proper

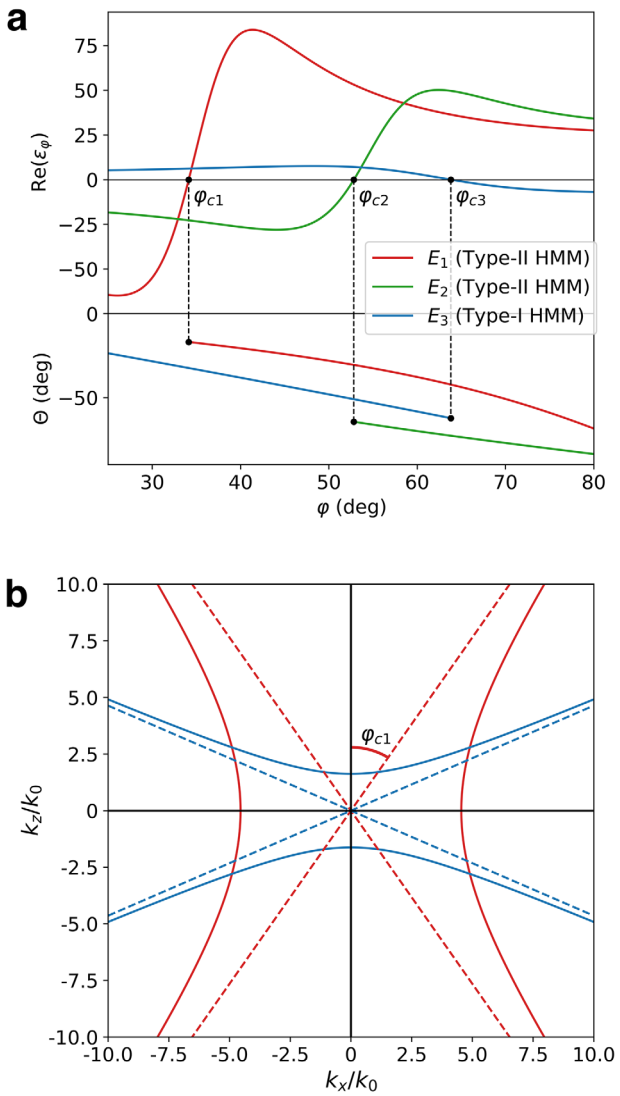

Figure 5. a) Real part of the angular dielectric function (ϵ_φ, top panel) and allowed conic angles (Θ, bottom panel) of excited VPPs with respect to optical axis for Si:InAs/AlSb multilayer (c_2 = 3.12%, f_m = 0.5) corresponding to the energies E_1, E_2, and E_3 shown in Figure 3; b) 2D projected *k*-dispersions for Si:InAs/AlSb (straight lines) corresponding to E_1 (Type-I, red lines) and E_2 (Type-II, blue lines). Dashed lines correspond to hyperboloid asymptotes whose slopes correspond to critical angles φ_c marked in panel a.

back-grating could facilitate the propagation of these modes outside the multilayer.

The VPP modes can be classified into distinct orders, based on the number of nodes in the magnetic field within the metamaterial (Figure 7, lower panel). VPP0 has zero nodes and represents the *0*-th order mode; VPP1 and VPP2 have one and two nodes and correspond to the *1*-st and *2*-nd order modes, respectively. The modulation of doping in the conductive layers further impacts the VPP modes (Figure 6b), by varying the hyperbolic ranges as well as the number and the energy position of the minima in the reflectivity. In particular, low-dopant concentration causes an overall flattening of the reflection spectrum, which indicates a higher energy loss of VPP modes. This implies that it exists a minimum doping level to effectively sustain plasmon-polariton waves across the multilayer.

This analysis confirms that this class of metamaterials may sustain hyperbolic dispersion and VPP propagation down to THz frequencies, while the details of the hyperbolic response critically depend on the number of layers and the grating geometry. For this reason, it is useful to calculate the photonic band structure of the periodically repeated multilayer, which provides the overall distribution of electromagnetic modes of the system (i.e., Bloch states). The results for Si:InAs/AlSb (c_2 = 3.12%, f_m = 0.5, d_{tot} = 100 nm) are summarized in **Figure 8**. Because of continuity conditions of the EM fields at the interface, the energy *E* and the wavefunction components parallel (k_x) and perpendicular (k_z) to the interface (Figure 1a) are not independent variables. In Figure 8a, the pixel colors in the grayscale spectrum represent the magnitude of the imaginary part of the complex Bloch wavevector k_z as a function of *E* and k_x. Lighter regions correspond to areas where the imaginary component is smaller, indicating less attenuation of electromagnetic waves within the

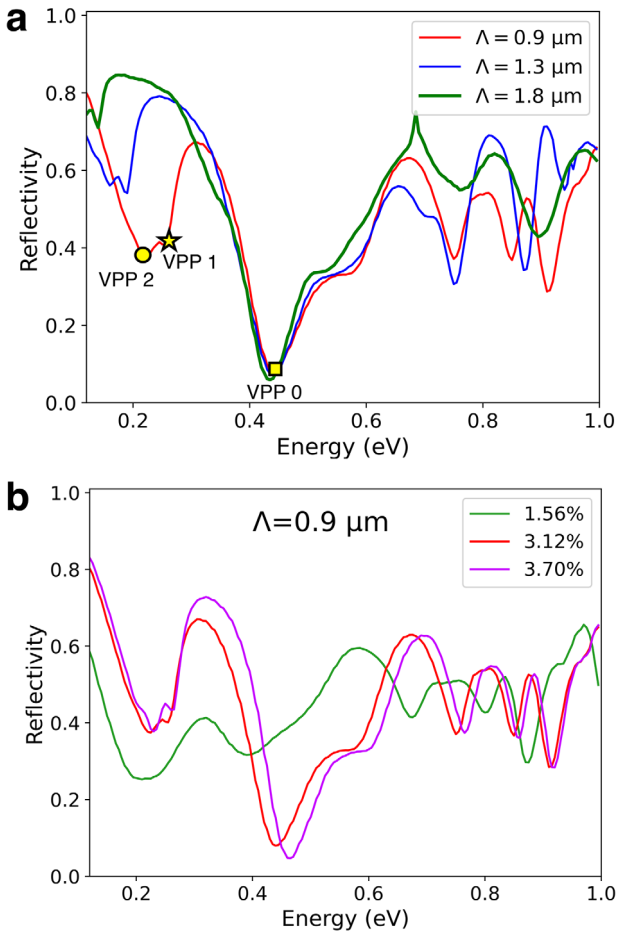

Figure 6. S-matrix simulations of reflectivity spectra (R) for Si:InAs/AlSb multilayers as a function of: a) grating periodicity (Λ); b) Si-doping concentration. Yellow square, star and circle correspond to VPP0, VPP1, and VPP2, respectively.

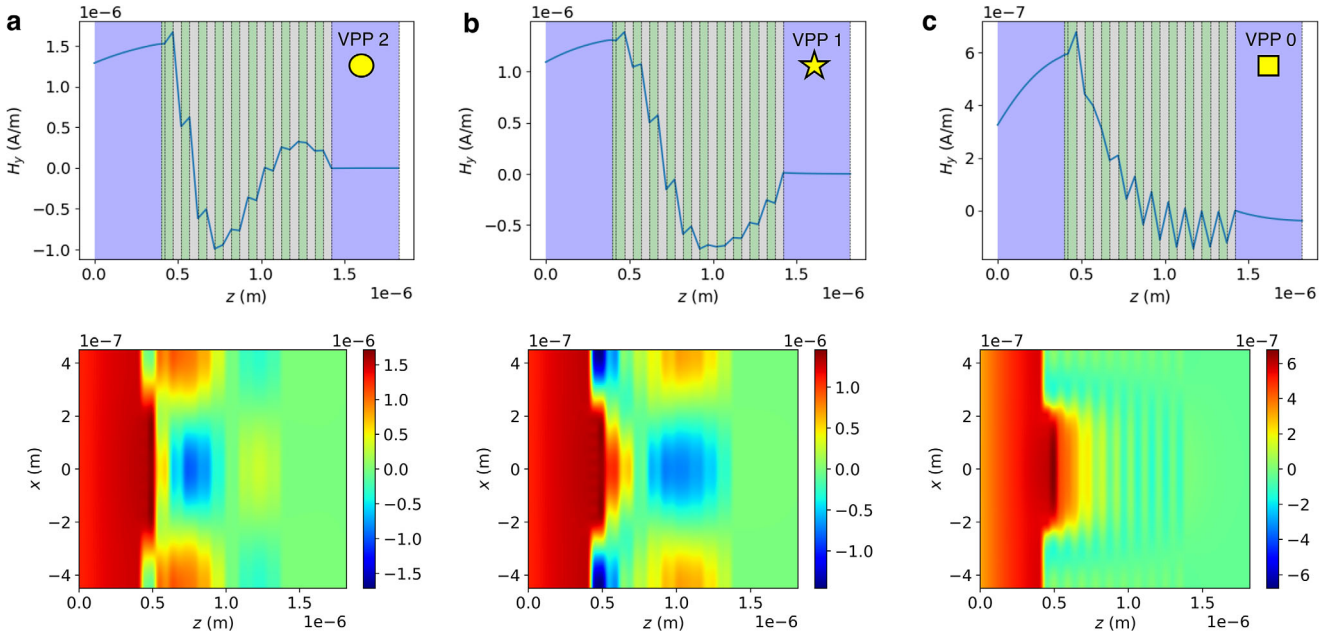

Figure 7. Magnetic field intensity (top) and 2D profile (bottom) of the a) VPP2, b) VPP1, and c) VPP0 modes identified in Figure 6a for Si:InAs/AlSb HMM ($c_2 = 3.12\%, f_m = 0.5, d_{tot} = 100$ nm, $\mathcal{N} = 10$, and $\Lambda = 0.9\mu$m). Green/gray areas identify metal/dielectric bilayers, violet areas mark the reflection/transmission embedding media (i.e., air); incoming light impinges on the left side of the multilayer, which includes also the grating layer. The 2D field profiles are computed with a spatial resolution of ≈11 nm along the x direction and ≈23 nm along the z direction.

metamaterial. Conversely, darker regions indicate higher attenuation due to a higher imaginary component.

While the PBS plot provides continuous solutions for the excitation of EM modes within the infinite multilayer, the application of boundary conditions due to finite-thickness stack and a matching coupler imposes selective rules, which restrict the possible VPP modes that can be excited in the metamaterial. For example, the inclusion of a grating layer imposes conditions on the in-plane k_x wavevectors, which depend on the grating periodicity Λ. For this reason, in Figure 8a we plotted the bandplot as a function of $\tilde{k}_x = k_x/T_x$, where $T_x = 2\pi/\Lambda$, and $\Lambda = 0.9\mu$m. This allows for the decomposition of grating refraction components in multiple harmonics, as shown in Figure 8b. The integer values $\tilde{k}_x = 0, 1, \ldots, n$ (vertical red lines) correspond to the fundamental, the first, ..., the n^{th} harmonic, respectively; the higher the harmonic, the lower the intensity of the refracted EM component.

In a similar way, the finite number of repeated metal/dielectric bilayers selects specific values for the possible k_z perpendicular to the stack. It is possible to excite just a finite number of Bloch waves in the multilayer, and this happens when the thickness of the stack is an integer multiple of half a wavelength of the incoming radiation. This corresponds to satisfy the resonance condition $d_{tot}/2\pi k_z = (m+1)/2\mathcal{N}$, where d_{tot} and $\mathcal{N}$ are the thickness and the number of the repeated bilayers, respectively, and m is an integer ranging from 0 to $\mathcal{N} - 1$. The m-index indicates the number of nodes of the EM field within the metamaterial and thus provides a direct correlation between the resonance values of k_z and the order of the VPP discussed above. Colored lines in Figure 8a represent the isovalue lines corresponding to the first six resonance k_z values for a Si:InAs/AlSb composed of $\mathcal{N} = 10$ bilayers. Once the grating and the thickness conditions are fixed, the intersections between the vertical red lines and the colored isolines correspond to the unique possible EM fields that may be excited within the metamaterials. Changing the values of Λ and/or $\mathcal{N}$ shifts the position of the matching points in the photonic band structure plot.

In the case of Figure 8a, for $E > 0.6$ eV the system has a dielectric character, thus the resonance points (cyan diamonds) correspond to the ordinary light refraction conditions. The values E = 0.74 and 0.89 eV at $\tilde{k}_x = 0$ closely match the higher energy minima in the reflectivity spectrum of Figure 6a. For $E \sim 0.5$ eV, the system has a Type-I hyperbolic response, and the matching point between the fundamental harmonic line $\tilde{k}_x = 0$ and the $m = 0$ isoline represents the VPP0 mode (yellow square), which corresponds to the lowest minimum in the reflectivity spectrum. The flat energy dispersion of the $m = 0$ isoline concurs with the insensitivity of the reflection minimum with respect to the grating periodicity Λ shown in Figure 6a. At lower energy, the system has a Type-II character. In this case, the fundamental harmonic does not contribute to higher order VPPs, i.e., no isoline intersections at $\tilde{k}_x = 0$. The VPP1 (yellow star) and VPP2 (yellow circle) resonances observed in reflection spectra mostly stem from the second harmonic diffraction peak ($\tilde{k}_x = 2$) and the isoline curves for $m = 1$ and $m = 2$. The proximity of these peaks to dark-color edge in the plot (i.e., higher energy dissipation) goes in parallel with the lower intensity of the corresponding reflection minima. Higher order VPPs could be further excited at higher harmonic conditions, but their low intensities make them hardly recognizable in the reflectivity spectra.

4. Conclusion

By combining multiscale and multiphysics techniques, we have investigated the possibility to excite and tune volume

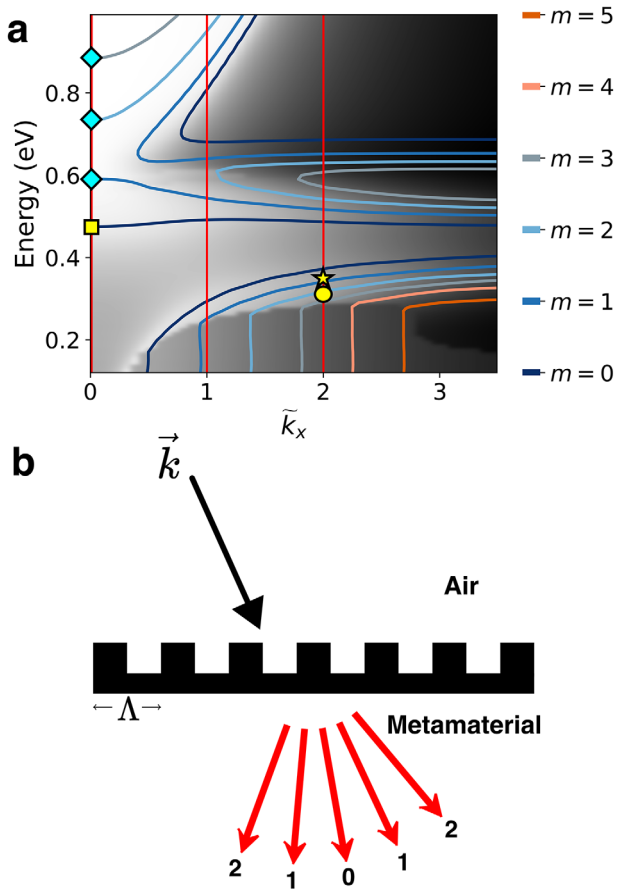

Figure 8. a) Photonic band structure of Si:InAs/AlSb ($c_2 = 3.12\%$, $f_m = 0.5$, $d_{tot} = 100$ nm). Red vertical lines correspond to the lowest harmonic contributions for $\Lambda = 0.9$ µm, colored curved lines correspond to the first six k_z resonance values ($m = \{0 - 5\}$) for $\mathcal{N} = 10$ metal/dielectric bilayers. Colored symbols indicate EM solutions for the selected geometric conditions: cyan diamonds correspond to ordinary dielectric refracted modes, yellow symbols indicate the most intense VPP modes as in Figure 6a. b) Schematic representation of harmonic generation from planar grating. Integer labels indicate the lowest diffracted harmonics and correspond to red lines in panel (a).

plasmon-polaritons modes in hyperbolic metamaterials based on III-V semiconductors. We analyzed the multi-dimensional phase space, by varying chemical composition, doping concentration, metallic filling factor, number of layers in the stack, and the grating coupler. This allows us to have a direct comparison with experiments and to gain a microscopic understanding of the origin of the volume plasmon-polaritons modes in these hyperbolic metamaterials. First principles simulations are used to evaluate the effect of doping on the dielectric function and the plasmonic excitation of the composing materials. While effective medium theory provides insights on the overall optical response of the metamaterials, the *S*-matrix approach is shown to be a powerful tool for interpreting experimental spectra, which keeps directly into account all the geometric features of the experimental setups. Finally, the photonic band structure is particularly useful to design and optimize the geometrical conditions to tune the energy and the spatial distribution of the volume plasmon-polaritons that may travel across the multilayer. Our integrated approach paves the way to a unique material-geometry co-design to realize optimal plasmon-based hyperbolic metamaterials. Starting from an atomistic description of the constituent materials, we demonstrate that the proper choice of composition and geometry setup allows for the excitation of multiple VPP traveling modes with high quality factors (i.e., low losses) across the mid-IR and THz ranges. Their energies and propagation lengths can be selectively controlled, opening new routes for bio-sensing applications, thermal emission control, and THz detection. In particular, the choice of III-V semiconductors (rather than noble metals) promises better compatibility with epitaxial growth, improving the monolithically integration with other semiconductor nanostructures (e.g., 2D materials, quantum wells, quantum dots, etc.), and the realization of novel hybrid polaritonic THz devices (e.g., on-chip optics, lasers, detectors, modulators) with enhanced performances and novel dispersion engineering. Furthermore, the high photonic density of states of HMMs, along with the plasmon tunability of doped-semiconductors make these systems promising for enhanced thermal emission and radiative thermal transfer, also beyond black-body limit.

Supporting Information

Supporting Information is available from the Wiley Online Library or from the author.

Acknowledgements

L.B. acknowledges financial support from PNRR MUR project ECS_00000033_ECOSISTER. A.C. acknowledges the National Centre for HPC, Big Data and Quantum Computing (ICSC), funded under the National Recovery and Resilience Plan (NRRP), Mission 04 Component 2 Investment 1.4, NextGenerationEU, Award Number:CN00000013. S.Cur. acknowledges support by the Office of Naval Research under grants N00014-23-1-2615 and N00014-24-1-2768, and by the DoD High Performance Computing Modernization Program (Frontier). S.Cur. also thanks Auro Scientific, LLC for computational support. The authors thank Drs. Simon Divilov, Xiomara Campilongo and Doug E. Wolfe for useful discussions.

Open access publishing facilitated by Consiglio Nazionale delle Ricerche, as part of the Wiley - CRUI-CARE agreement.

Conflict of Interest

The authors declare no conflict of interest.

Author Contributions

A.C. and L.B. conceptualized the work. S.C. performed calculations and implemented the AFLOW-EMERALD code. S.C., L.B., and A.C. analyzed data. A.C. and S. Cur. established the research direction and supervised the project. All the authors contributed to the writing of the manuscript.

Data Availability Statement

The data that support the findings of this study are available from the corresponding author upon reasonable request.

Keywords

III-V semiconductors, hyperbolic metamaterials, THz plasmonics

Received: August 14, 2025
Revised: December 11, 2025
Published online: January 23, 2026

[1] I. I. Smolyaninov, *Hyperbolic Metamaterials*, Morgan & Claypool Publishers, **2018**, pp. 2053–2571.
[2] A. Poddubny, I. Iorsh, P. Belov, Y. Kivshar, *Nature Phot.* **2013**, *7*, 948.
[3] K. Sreekanth, A. De Luca, G. Strangi, *J. Opt.* **2014**, *16*, 105103.
[4] A. Moradi, *Theory of Electrostatic Waves in Hyperbolic Metamaterials*, Springer Series in Optical Sciences, **2023**.
[5] S. V. Zhukovsky, O. Kidwai, J. E. Sipe, *Opt. Express* **2013**, *21*, 14982.
[6] L. Ferrari, C. Wu, D. Lepage, X. Zhang, Z. Liu, *Prog. Quantum Electron.* **2015**, *40*, 1.
[7] K. V. Sreekanth, Y. Alapan, M. ElKabbash, A. M. Wen, E. Ilker, M. Hinczewski, U. A. Gurkan, N. F. Steinmetz, G. Strangi, *Adv. Opt. Mater.* **2016**, *4*, 1767.
[8] A. Kumar, N. Kumar, G. N. Pandey, D. Singh, K. B. Thapa, *J. Phys.: Cond. Mat.* **2020**, *32*, 325701.
[9] X. Yin, C. Long, J. Li, H. Zhu, L. Chen, J. Guan, X. Li, *Sci. Rep.* **2015**, *5*, 15367.
[10] E. E. Narimanov, H. Li, Y. A. Barnakov, M. A. Noginov, In *Conference on Lasers and Electro-Optics 2010* Optica Publishing Group, **2010**, QPDA6.
[11] S.-A. Biehs, M. Tschikin, P. Ben-Abdallah, *Phys. Rev. Lett.* **2012**, *109*, 104301.
[12] Y. Guo, Z. Jacob, *Opt. Express* **2013**, *21*, 15014.
[13] P. Shekhar, J. Atkinson, Z. Jacob, *Nano Converg.* **2014**, *1*, 1.
[14] G. V. Naik, J. Liu, A. V. Kildishev, V. M. Shalaev, A. Boltasseva, *Proc. Nat. Acad. Sci.* **2012**, *109*, 8834.
[15] G. V. Naik, V. M. Shalaev, A. Boltasseva, *Proc. Nat. Acad. Sci.* **2014**, *111*, 7546.
[16] H. Nan, P. Xiong, G.-J. Zhong, Y. Li, R. Li, J.-H. Niu, J. Lei, Z.-M. Li, *ACS Appl. Nano Mater.* **2024**, *7*, 1711.
[17] Y. J. Jen, T.-L. Chan, *Opt. Express* **2023**, *31*, 7734.
[18] C. T. Riley, J. S. T. Smalley, J. R. J. Brodie, Y. Fainman, D. J. Sirbuly, Z. Liu, *Proc. Nat. Acad. Sci.* **2017**, *114*, 1264.
[19] Q. Ma, H. Qian, S. Montoya, W. Bao, L. Ferrari, H. Hu, E. Khan, Y. Wang, E. E. Fullerton, E. E. Narimanov, X. Zhang, Z. Liu, *ACS Nano* **2018**, *12*, 11316.
[20] Y. U. Lee, J. Zhao, Q. Ma, L. K. Khorashad, C. Posner, G. Li, G. B. M. Wisna, Z. Burns, J. Zhang, Z. Liu, *Nature Commun.* **2021**, *12*, 1559.
[21] A. J. Hoffman, L. Alekseyev, S. S. Howard, K. J. Franz, D. Wasserman, V. A. Podolskiy, E. E. Narimanov, D. L. Sivco, C. Gmachl, *Nature Mater.* **2007**, *6*, 946.
[22] A. Boltasseva, H. A. Atwater, *Science* **2011**, *331*, 290.
[23] M. Karaliūnas, K. E. Nasser, A. Urbanowicz, I. Kašalynas, D. Bražinskienė, S. Asadauskas, G. Valušis, *Sci. Rep.* **2018**, *8*, 18025.
[24] A. Gong, Y. Qiu, X. Chen, Z. Zhao, L. Xia, Y. Shao, *Appl. Spectr. Rev.* **2020**, *55*, 418.
[25] C. Jansen, S. Wietzke, O. Peters, M. Scheller, N. Vieweg, M. Salhi, N. Krumbholz, C. Jördens, T. Hochrein, M. Koch, *Appl. Opt.* **2010**, *49*, E48.
[26] A. G. Davies, A. D. Burnett, W. Fan, E. H. Linfield, J. E. Cunningham, *Mater. Today* **2008**, *11*, 18.
[27] H. Chen, L. Shao, Q. Li, J. Wang, *Chem. Soc. Rev.* **2013**, *42*, 2679.
[28] W. Li, U. Guler, N. Kinsey, G. V. Naik, A. Boltasseva, J. Guan, V. M. Shalaev, A. V. Kildishev, *Adv. Mater.* **2014**, *26*, 7959.
[29] A. Catellani, A. Calzolari, *Phys. Rev. B* **2017**, *95*, 115145.
[30] A. Calzolari, A. Catellani, M. Buongiorno Nardelli, M. Fornari, *Adv. Opt. Mater.* **2021**, *9*, 2001904.
[31] A. Calzolari, C. Oses, C. Toher, M. Esters, X. Campilongo, S. P. Stepanoff, D. E. Wolfe, S. Curtarolo, *Nature Commun.* **2022**, *13*, 5993.
[32] S. Divilov, S. Griesemer, R. C. Koennecker, M. Ammendola, A. Zettel, H. Eckert, J. Shallenberger, X. Campilongo, W. Fahrenholtz, A. Calzolari, D. E. Wolfe, S. Curtarolo, *High Entropy Alloys & Materials* **2025**, *3*, 273.
[33] G. S. Rohrer, M. Affatigato, M. Backhaus, R. K. Bordia, H. M. Chan, S. Curtarolo, A. Demkov, J. N. Eckstein, K. T. Faber, J. E. Garay, Y. Gogotsi, L. Huang, L. E. Jones, S. V. Kalinin, R. J. Lad, C. G. Levi, J. Levy, J.-P. Maria, L. Mattos Jr, A. Navrotsky, N. Orlovskaya, C. Pantano, J. F. Stebbins, T. S. Sudarshan, T. Tani, K. S. Weil, *J. Am. Ceram. Soc.* **2012**, *95*, 3699.
[34] H. R. Seren, J. Zhang, G. R. Keiser, S. J. Maddox, X. Zhao, K. Fan, S. R. Bank, X. Zhang, R. D. Averitt, *Light: Science & Applications* **2016**, *5*, e16078.
[35] J. Tong, F. Suo, T. Zhang, Z. Huang, J. Chu, D. H. Zhang, *Light: Science & Applications* **2021**, *10*, 58.
[36] I. Aupiais, R. Grasset, T. Guo, D. Daineka, J. Briatico, S. Houver, L. Perfetti, J.-P. Hugonin, J.-J. Greffet, Y. Laplace, *Nature Commun.* **2023**, *14*, 7645.
[37] J. Duan, M. O. Liedke, W. Dawidowski, R. Li, M. Butterling, E. Hirschmann, A. Wagner, M. Wang, L. B. Young, Y.-H. G. Lin, M. Hong, M. Helm, S. Zhou, S. Prucnal, *J. Appl. Phys.* **2023**, *134*, 095102.
[38] D. Li, C. Z. Ning, *Opt. Express* **2011**, *19*, 14594.
[39] J. Chochol, K. Postava, M. Čada, M. Vanwolleghem, M. Mičica, L. Halagačka, J.-F. Lampin, J. Pištora, *J. Eur. Opt. Soc. Rapid Publ.* **2017**, *13*, 13.
[40] X. Wang, A. A. Belyanin, S. A. Crooker, D. M. Mittleman, J. Kono, *Nature Phys.* **2010**, *6*, 126.
[41] P. Sai, V. V. Korotyeyev, M. Dub, M. Słowikowski, M. Filipiak, D. B. But, Y. Ivonyak, M. Sakowicz, Y. M. Lyaschuk, S. M. Kukhtaruk, G. Cywiński, W. Knap, *Phys. Rev. X* **2023**, *13*, 041003.
[42] P. Sohr, D. Wei, S. Tomasulo, M. K. Yakes, S. Law, *ACS Photonics* **2018**, *5*, 4003.
[43] P. Sohr, D. Wei, Z. Wang, S. Law, *Nano Lett.* **2021**, *21*, 9951.
[44] M. Desouky, A. M. Mahmoud, M. A. Swillam, *Sci. Rep.* **2017**, *7*, 15312.
[45] S. Jahani, Z. Jacob, *Nature Nanotech.* **2016**, *11*, 23.
[46] D. Wei, C. Harris, C. C. Bomberger, J. Zhang, J. Zide, S. Law, *Opt. Express* **2016**, *24*, 8735.
[47] S. Q. Li, P. Guo, L. Zhang, W. Zhou, T. W. Odom, T. Seideman, J. B. Ketterson, R. P. H. Chang, *ACS Nano* **2011**, *5*, 9161.
[48] W. Liang, Z. Li, Y. Wang, W. Chen, Z. Li, *Photon. Res.* **2019**, *7*, 318.
[49] H. M. K. Wong, A. S. Helmy, *J. Opt. Soc. Am. B* **2013**, *30*, 1000.
[50] F. Caruso, F. Giustino, *Phys. Rev. B* **2016**, *94*, 115208.
[51] J.-M. Lihm, C.-H. Park, *Phys. Rev. Lett.* **2024**, *133*, 116402.
[52] H. Zhang, V. Kulkarni, E. Prodan, P. Nordlander, A. O. Govorov, *J. Phys. Chem. C* **2014**, *118*, 16035.
[53] J. Jung, T. G. Pedersen, *J. Appl. Phys.* **2013**, *113*, 114904.
[54] J. Gjerde, R. A. Jishi, *Comput. Mater. Sci.* **2023**, *226*, 112199.
[55] A. Ebrahimian, R. Asgari, *Phys. Rev. B* **2021**, *103*, 035425.
[56] M. N. Gjerding, R. Petersen, T. G. Pedersen, N. A. Mortensen, K. S. Thygesen, *Nature Commun.* **2017**, *8*, 320.
[57] P. Giannozzi, S. Baroni, N. Bonini, M. Calandra, R. Car, C. Cavazzoni, D. Ceresoli, G. L. Chiarotti, M. Cococcioni, I. Dabo, A. D. Corso, S. de Gironcoli, S. Fabris, G. Fratesi, R. Gebauer, U. Gerstmann, C. Gougoussis, A. Kokalj, M. Lazzeri, L. Martin-Samos, N. Marzari, F. Mauri, R. Mazzarello, S. Paolini, A. Pasquarello, L. Paulatto, C. Sbraccia, S. Scandolo, G. Sclauzero, A. P. Seitsonen, et al., *J. Phys.: Condens. Matter* **2009**, *21*, 395502.
[58] P. Giannozzi, O. Andreussi, T. Brumme, O. Bunau, M. B. Nardelli, M. Calandra, R. Car, C. Cavazzoni, D. Ceresoli, M. Cococcioni, N. Colonna, I. Carnimeo, A. D. Corso, S. de Gironcoli, P. Delugas, R. A. DiStasio, A. Ferretti, A. Floris, G. Fratesi, G. Fugallo, R. Gebauer, U. Gerstmann, F. Giustino, T. Gorni, J. Jia, M. Kawamura, H.-Y. Ko, A. Kokalj, E. Küçükbenli, M. Lazzeri, et al., *J. Phys.: Condens. Matter* **2017**, *29*, 465901.

[59] J. P. Perdew, K. Burke, M. Ernzerhof, *Phys. Rev. Lett.* **1996**, *77*, 3865.
[60] D. R. Hamann, *Phys. Rev. B* **2013**, *88*, 085117.
[61] Pseudopotential library, https://github.com/pipidog/ONCVPSP, **2022**.
[62] S. L. Dudarev, G. A. Botton, S. Y. Savrasov, C. J. Humphreys, A. P. Sutton, *Phys. Rev. B* **1998**, *57*, 1505.
[63] B. Himmetoglu, A. Floris, S. De Gironcoli, M. Cococcioni, *Int. J. Quantum Chem.* **2014**, *114*, 14.
[64] L. A. Agapito, S. Curtarolo, M. Buongiorno Nardelli, *Phys. Rev. X* **2015**, *5*, 011006.
[65] M. Buongiorno Nardelli, F. T. Cerasoli, M. Costa, S. Curtarolo, R. De Gennaro, M. Fornari, L. Liyanage, A. R. Supka, H. Wang, *Comput. Mater. Sci.* **2018**, *143*, 462.
[66] A. Calzolari, A. Ruini, A. Catellani, *ACS Photonics* **2014**, *1*, 703.
[67] R. Colle, P. Parruccini, A. Benassi, C. Cavazzoni, *J. Phys. Chem. B* **2007**, *111*, 2800.
[68] F. Wooten, *Optical Properties of Solids*, Academic Press, New York and London, **1972**.
[69] O. Kidwai, S. V, J. E. Sipe, *Phys. Rev. A* **2012**, *85*, 053842.
[70] D. W. Berreman, *J. Opt. Soc. Am.* **1972**, *62*, 502.
[71] R. C. Rumpf, *Prog. Electr. Res. B* **2011**, *35*, 241.
[72] M. Born, E. Wolf, A. B. Bhatia, P. C. Clemmow, D. Gabor, A. R. Stokes, A. M. Taylor, P. A. Wayman, W. L. Wilcock, *Principles of Optics: Electromagnetic Theory of Propagation, Interference and Diffraction of Light*, 7th Edition, Cambridge University Press, Cambridge, UK **1999**.
[73] S. Campanaro, L. Bursi, S. Curtarolo, A. Calzolari, *AFLOW-EMERALD-ElectroMagnetic Modes EngineeRing in Advanced LayereD Materials Preprint* **2025**.
[74] M. Agio, L. Andreani, F. Bassani, G. L. Liedl, P. Wyder, editors, *Encyclopedia of Condensed Matter Physics*, Elsevier, Oxford, **2005**, pp. 286–294.
[75] Y.-S. Kim, K. Hummer, G. Kresse, *Phys. Rev. B* **2009**, *80*, 035203.
[76] Y.-S. Kim, M. Marsman, G. Kresse, F. Tran, P. Blaha, *Phys. Rev. B* **2010**, *82*, 205212.
[77] J. Even, L. Pedesseau, E. Tea, S. Almosni, A. Rolland, C. Robert, J.-M. Jancu, C. Cornet, C. Katan, J.-F. Guillemoles, O. Durand, *Int. J. Photoenergy* **2014**, *2014*, 649408.
[78] G. Grosso, G. P. Parravicini, *Solid State Physics*, Academic press, Cambridge, Massachusetts, **2013**.
[79] S. H. Rhim, M. Kim, A. J. Freeman, R. Asahi, *Phys. Rev. B* **2005**, *71*, 045202.
[80] S. Hwang, T. Kim, Y. Jung, N. Barange, H. Park, J. Kim, Y. Kang, Y. Kim, S. Shin, J. Song, C.-T. Liang, Y.-C. Chang, *J. Alloys Comp.* **2014**, *587*, 361.
[81] M. Garriga, P. Lautenschlager, M. Cardona, K. Ploog, *Sol. St. Commun.* **1987**, *61*, 157.
[82] S. Zollner, C. Lin, E. Schönherr, A. Böhringer, M. Cardona, *J. Appl. Phys.* **1989**, *66*, 383.
[83] I. V. Lindell, S. A. Tretyakov, K. I. Nikoskinen, S. Ilvonen, *Microwave Opt. Tech. Lett.* **2001**, *31*, 129.